# Plate-style recuperator for a solar Brayton cycle using high-temperature sealant

**Kyle E. Dellar, Willem G. le Roux* and Josua P. Meyer**

Department of Mechanical and Aeronautical Engineering, University of Pretoria,
Private Bag X20, Hatfield, 0028, South Africa
*Corresponding author: willem.leroux@up.ac.za

## Highlights

- Sodium silicate-based sealant was investigated for use in a recuperator.
- Small-scale clamped plate-style recuperator designs were built and tested.
- A cold-side effectiveness of 82.5% was found for the recuperator core in experiment.
- A total pressure loss of 24.9 kPa was found for the recuperator core in experiment.
- A validated mathematical model was applied to a solar Brayton cycle recuperator.

## Abstract

A large, efficient recuperator is required for high cycle efficiency in a solar Brayton cycle (STBC) with an open-cavity solar receiver and air as working fluid. A recuperator often requires complex and costly manufacturing methods. In this work, a clamped plate-type recuperator with a metal gasket is investigated, together with a low-cost high-temperature sodium silicate-based sealant. Experimental investigations were performed to validate a mathematical model using a novel bone-shape design as well as a wide-channel design. The high-temperature sealant worked well on the bone-shape recuperator; however, a leak occurred on the hot-side header tube of the wide-channel recuperator. For the recuperator core of the wide-channel test rig, a cold-side effectiveness of 82.5% and a total pressure loss of 24.9 kPa were found at an average mass flow rate of 0.74 g/s per channel. The validated mathematical model was used in a parametric study to analyse the performance of the recuperator in an STBC by taking the stress and deflection of the plates into consideration. Results show that, for a total mass flow rate of 0.06 kg/s, a cold-side effectiveness of 90% and total pressure loss of less than 5% could be achieved, if a spacer is implemented to prevent deflection.

*Keywords: Recuperator; Sodium silicate; Sealant; Counterflow; Plate-type; Brayton.*

## 1. Introduction

Renewable energy is in ever-increasing demand, with solar energy being one of the front-runners. Solar energy is classified into two main categories, namely photovoltaics (PV) and concentrating solar power (CSP) [1]. One form of a CSP system is a central receiver design

whereby a large array of heliostats (reflective mirrors) focuses the sun's direct normal irradiance (DNI) onto a single point [2]. When this system is downscaled and made more compact, the heliostats is replaced by a parabolic solar dish reflector, which concentrates the DNI onto a cavity receiver [3,4]. The highly concentrated solar flux can then be used as the heat source for a micro-turbine in a Brayton cycle, creating what is referred to as a solar thermal Brayton cycle (STBC). McDonald and Rodgers [5] state that personal micro-turbine power generation systems may be as commonplace in the future as owning a personal computer. They suggest that a compact, gas-fired, silent-running personal micro-turbine with very low emissions would operate unattended and would be essentially maintenance-free, resulting in generator sets having the potential to become standard items in new homes in coming decades. Such a micro-turbine, driven by concentrated solar power (using a solar dish), is an attractive option when considering smaller-scale applications where space is not a restriction. The STBC allows for low costs [6], high reliability [7], simplicity, reduced water consumption, and the use of air as working fluid. The STBC has been shown to operate at efficiencies from 11.76% [8] and thermal efficiencies of up to 30% [9] while maintaining turbine inlet temperatures in the region of 760 °C to 871 °C [7].

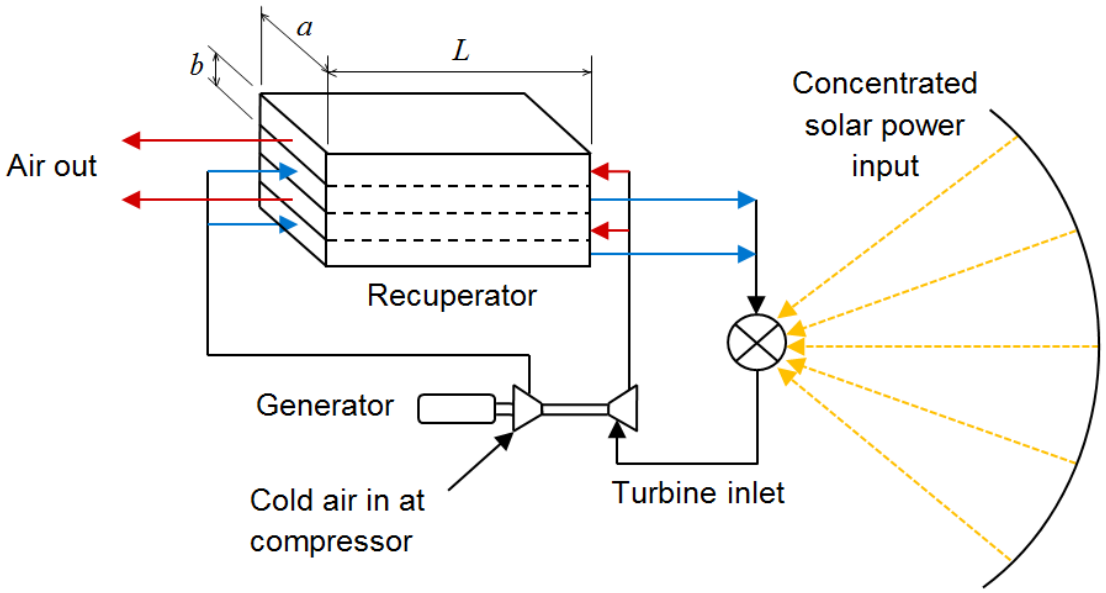


**Fig. 1.** A recuperated solar thermal Brayton cycle (not drawn to scale).

Fig. 1 shows a cycle diagram for an STBC. The dimensions of the solar receiver and recuperator in a small-scale (1-20 kW) dish-mounted STBC have been optimised by Le Roux [10,11], using the method of entropy generation minimisation. A prototype is proposed to generate mechanical power by reflecting solar irradiance with a 4.8 m reflective dish onto an open-cavity tubular receiver [12], at solar to mechanical efficiencies ranging from 10% to 20% [13]. The means by which it can extract the thermal energy and convert it to kinetic energy is via the implementation

of a micro gas turbine in the form of a turbocharger from the automotive industry. Turbochargers are readily available and thus affordable [14], and have been developed for many decades to perform well at the proposed operating conditions of up to 950 °C [15]. To continue generating power during periods of sparse or no solar irradiance, thermal storage methods such as packed rock bed [16] and molten metal systems [17,18] have been investigated. The addition of a combustion chamber to hybridise the cycle is a well-known solution for continuous operation [19]; it can utilise a wide range of fuels including hydrogen [20]. Another means of improving the utilisation of the cycle's energy is by capturing the exhausted heat and putting it to use in applications such as water heating [14,19], absorption chilling or desalination. The purpose of the small-scale STBC is to create a mobile, easily deployable, off-grid source of electricity and hot water to communities in need of such resources.

In order for the STBC to operate at moderate to high efficiencies with the implementation of a turbocharger, the recuperator shown in Fig. 1 is key. The recuperator removes heat from the gas exiting the turbine and transfers it to the air stream exiting the compressor, allowing for a less complex solar receiver. The recuperator is a high-temperature heat exchanger, usually operating at temperatures of above 650 °C [21], and allows for less external heat input (fuel or solar irradiance) in addition to lowering the required pressure ratios (typically three to four times lower than those of a non-recuperated cycle) [15]. McDonald [22] provides typical criteria for a recuperator to be beneficial to the cycle, which are as follows: low manufacturing cost, high reliability, high effectiveness (> 90%) and a low pressure loss (< 5%). Following these criteria, a counterflow design is required.

The main heat exchanger categories which encompass recuperators are tubular, plate-type (also known as primary-surface recuperators), and plate-fin, which falls under the extended surface category [23]. Clay and Tansley [24] have developed and analysed a tubular recuperator. The design manages a cold-side effectiveness of 76%, with a total pressure loss in the region of 15%. Although the tubular design allows for a low-cost solution, the performance is heavily affected. Xiao et al. [23] compare various typical recuperator solutions that manufacturers have provided. Plate-type and plate-fin recuperators are the most widely implemented because of their ability to achieve high effectiveness values and low pressure losses in addition to remaining compact. McDonald [25] suggests that a plate-fin counterflow iteration is necessary. However, according to Scaccia and Theoclitus [26], fins should be avoided within a Brayton cycle recuperator due to the increased likelihood of fouling, as well as the negligible effect of fins in such a recuperator relative to the cost and weight. Fouling can become a major concern for recuperators regardless of the geometry, especially when incomplete combustion takes place. Besides the insulative effects that deposition-type fouling can cause, with soot-based fouling having thermal conductivities ranging from 0.02 W/m.°C to 1 W/m.°C, there can be significant pressure loss increases due to the reduction in flow area and rough character of the deposit [27].

Developing a recuperator that adheres to the criteria of McDonald [22] whilst remaining cost-effective is a challenge. According to McDonald [22], a recuperator represents up to 30% of the

capital cost of a micro-turbine package. Recuperator manufacturing methods usually involve expensive processes such as furnace brazing, laser welding and metallic 3D printing. An example of such a plate-type recuperator is presented by Kesseli et al. [28], with a cold-side effectiveness of 90% and a pressure loss of 5% [23]. The body is constructed from plates and gaskets which are stacked and then furnace brazed together to form a seal. Furthermore, Cordova et al. [29] propose a more complex radial configuration recuperator for oil-free turbogenerators, which could achieve an effectiveness of over 90%. A novel Swiss-roll recuperator has also been investigated [30,31].

Ohadi and Buckley [32] have listed the main potential materials which could be used for high-temperature recuperator applications as well as the material properties. Le Roux and Sciacovelli [18] have shown that the STBC can also operate at lower receiver operating temperatures of about 600 °C, which have an advantage in terms of cost because stainless steel materials can be used instead of super-alloys for recuperator inlet temperatures of less than 670 °C [15]. Gasketed plate-type heat exchangers are often used for lower temperature applications [33] because of material limits, and they are usually operated below 150 °C to avoid the use of expensive gasket materials [34]. However, high thermal performance can be achieved in counterflow plate-type heat exchangers [34].

In this work, the utilisation of a counterflow clamped plate-type recuperator with a metal gasket is investigated, together with a low-cost high-temperature sodium silicate-based sealant. The sealant is designed for the sealing of joints and openings in high-temperature applications at temperatures of up to 1500 °C [35]. The effectiveness and pressure drop characteristics of the recuperator using the sodium silicate-based sealant are considered. Two experimental investigations are performed to validate a mathematical model on two different small-scale test rigs, based on a novel bone-shape design as well as a wide-channel design. The novelty of the designs stems from the objective of manufacturing the recuperator at a relatively low cost using readily available material. The mathematical model is used to analyse the performance of a full-scale recuperator for operation in an STBC by taking the stress and deflection of the plates into consideration.

## 2. Mathematical model

The effectiveness-*NTU* method was employed to analyse and create a model of the proposed counterflow plate-style recuperator. Fig. 1 shows the basic layout on which the calculations were based, whereby a single channel was considered for each fluid flow stream. Note that $a$ is the channel width, $b$ the channel height, $L$ the channel length, and $t$ the plate thickness between channels.

Fig. 2 (left) depicts a schematic of a novel bone-shape plate-style counterflow recuperator design. The proposed design has been generated to fulfil the requirements of cost-effectiveness and ease of assembly. Its construction relies on the repetition of alternating plates and gaskets,

which can be laser cut from metal sheet. Each plate is identical, and so is each gasket. The gaskets are then inverted for each placement to create separate hot and cold fluid flow paths. The plate-gasket layers can then be stacked ad infinitum to generate a recuperator with the desired number of channels. Additionally, the channel height, *b*, can be changed by selecting a metal sheet of the desired thickness. Once stacked to create a recuperator of the specified size, the assembly can be sandwiched between two thick plates and squeezed together via bolts around the periphery of the unit. To ensure that no leakage occurs, a high-temperature sodium silicate-based sealant [35] can be instituted between the plates and gaskets. Fig. 2 (right) details the layout of the gasket plate arrangement by showing an exploded view of the recuperator. The alternating hot and cold channels are shown, revealing how the fluid streams follow a counterflow path.

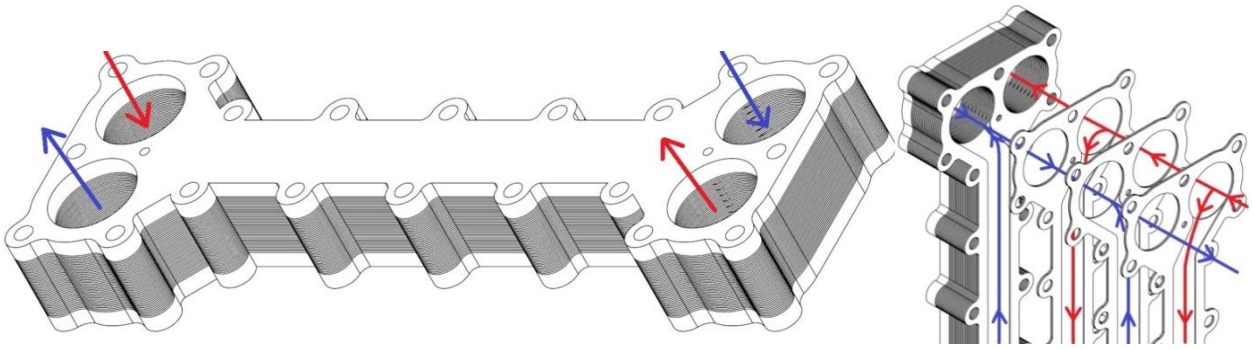

**Fig. 2.** Plate-style counterflow recuperator concept (left), and exploded view of recuperator concept (right).

### *2.1. Heat transfer calculation*

The main calculations for the number of transfer units (*NTU*) and the effectiveness are shown in Eqs. (1), (2) and (3) [36].

$$NTU = \frac{A_s}{C_{p,c}\,\dot{m}_{channel}\left[\frac{2ab}{\mathrm{Nu}(a+b)}\left(\frac{1}{k_c}+\frac{1}{k_h}\right)+R_{f,h}+R_{f,c}+\frac{t}{k_{steel}}\right]} \tag{1}$$

$$\varepsilon = \frac{c - ce^{\left[-NTU\left(1-\frac{1}{c}\right)\right]}}{c - e^{\left[-NTU\left(1-\frac{1}{c}\right)\right]}} \tag{2}$$

$$c = C_{p,h}/C_{p,c} \tag{3}$$

Equation (1) is specific to the design because it is representative of a recuperator with channels operating within a laminar, fully developed flow regime. Due to this operating state, the Nusselt number, Nu = 8.24, is constant for the specific channel geometry where $a/b \gg 8$ [36]. This Nusselt number is slightly conservative because the average Nusselt number will be higher due to the developing flow region, which will enhance heat transfer [37], and because mixed convection will occur [38]. However, the entry length of the recuperator channels is relatively short [36] with a negligible increase in the average Nusselt number. The fouling factor for the clean air on the cold side is taken to be $R_{f,c}$ = 0.0004 m$^2$.°C/W [36]. The fouling factor for the hot side is taken to be $R_{f,h}$ = 0.0006 m$^2$.°C/W [36], due to the combustion of LPG, which only introduces a small amount of water vapour and $CO_2$ when combusted stoichiometrically. The fouling factor for the hot side could be different for the experimental validation as a result of incomplete combustion leading to large soot deposits. The heat loss analysis conducted for the recuperator design is based on calculations shown in previous work [39-41]. To calculate the hot and cold-side effectiveness values for a counterflow heat exchanger with heat loss, Eqs. (4) and (5) are employed (adapted from Nellis and Pfotenhauer [42]):

$$\varepsilon_h = \begin{cases} 1-\theta_{X=1}, & c<1 \\ c(1-\theta_{X=1}), & c>1 \end{cases} \tag{4}$$

$$\varepsilon_c = \begin{cases} (1-\theta_{X=0})/c, & c<1 \\ 1-\theta_{X=0}, & c>1 \end{cases} \tag{5}$$

The dimensionless temperature difference is calculated using Eqs. (6) and (7), where the number of transfer units is calculated using Eq. (8).

$$\theta_{X=0} = \frac{\left(\frac{\left(\dot{Q}_c+\dot{Q}_h\right)(c-1)}{c\dot{Q}_{\max}}\right)+\frac{(c-1)^2}{c}+\left(\frac{\dot{Q}_h+c\dot{Q}_c}{UA_s\left(T_{h,in}-T_{c,in}\right)}\right)\left(1-e^{NTU_h(c-1)}\right)}{\left(\frac{c-1}{c}\right)\left(ce^{NTU_h}-1\right)} \tag{6}$$

$$\theta_{X=1} = \left(\frac{\dot{Q}_c+\dot{Q}_h}{c\dot{Q}_{\max}}\right)+\frac{\left(\theta_{X=0}-1\right)}{c}+1 \tag{7}$$

$$NTU_h = \frac{UA_s}{\dot{m}C_{p,h}} \tag{8}$$

The heat transfer rates are calculated as shown in Eqs. (9), (10) and (11).

$$\dot{Q}_{max} = \dot{m}C_{p,c}(T_{h,i} - T_{c,i}) \tag{9}$$

$$\dot{Q}_h = \dot{m}C_{p,h}(T_{h,i} - T_{h,o}) \tag{10}$$

$$\dot{Q}_c = \dot{m}C_{p,c}(T_{c,o} - T_{c,i}) \tag{11}$$

*2.2. Pressure drop analysis*

Equation (13) is derived from Eq. (12) to determine the pressure drop in a specific channel [36], while Eq. (14) (integrated to account for variable mass flow rate over the inlet and outlet sections) allows for the pressure drop to be found in the inlet and outlet header tubes that feed the channels. This approach is necessary because the fluid mass flow rate decreases linearly as the fluid flows further into the inlet header tube, being distributed among the channels, and vice versa when the fluid accumulates linearly as the fluid flows towards the exit of the outlet header tube.

$$\Delta P = \frac{fL}{D_h} \cdot \frac{\rho V^2}{2} \tag{12}$$

$$\Delta P_{channel} = \frac{fL(\dot{m}_{channel})^2(a+b)}{4\rho(ab)^3} \tag{13}$$

$$\Delta P_{headertube} = \frac{1}{L}\int_0^L \frac{f \cdot x}{D_t} \cdot \frac{[\dot{m}(x)]^2}{2\rho A^2} dx = \frac{4f(\dot{m}_{tot})^2(N[b+t])}{3\pi^2\rho(D_t)^5} \tag{14}$$

where

$$\dot{m}(x) = -\frac{\dot{m}_{tot}}{2N[b+t]} \cdot x + \dot{m}_{tot} \tag{15}$$

The total pressure drop for the entire recuperator in the STBC (see Fig. 1) is simply a summation of the inlet and outlet header tube pressure drop, as well as the channel pressure drop, for both the hot and cold sides, as shown in Eq. (16).

$$\Delta P_{tot} = \Delta P_{headertube,c} + \Delta P_{headertube,h} + \Delta P_c + \Delta P_h \tag{16}$$

*2.3 Stress analysis*

Equation (17) calculates the stress, while Eq. (18) calculates the maximum deflection [43] of a recuperator channel plate due to the pressure differential from the high pressure (cold) side and the low pressure (hot) side, as shown in Fig. 1. $\Delta P_{avg}$ is the average pressure difference across a recuperator channel plate which separates a hot channel from a cold channel, while the Young's modulus, $E$, is evaluated at the operational temperature of the plate. Note that the channel height, $b$, is adjusted according to the deflection.

$$\sigma_{max} = \frac{-0.5\Delta P_{avg}(a)^2}{t^2} \tag{17}$$

$$y_{max} = \frac{0.0284\ \Delta P_{avg}(a)^4}{Et^3} \tag{18}$$

## 3. Experimental setup

Two separate tests with different recuperator designs were conducted in order to acquire a range of data for differing geometries and fluid conditions.

*3.1. Test 1 – Mark I rig*

The Mark I design, which was generated from the theoretical model and manufactured from mild steel, is shown in Fig. 3. The dimensions were determined iteratively during the early stages of the model's development by aiming for an effectiveness as close to 90% as possible while remaining within size and weight constraints to which a working prototype would have to adhere when attached to the small-scale STBC prototype [12]. The pressure loss and plate deflection values also played a role in the design. Fig. 4 displays the Mark I test rig during assembly with the sodium-silicate sealant (Calofer) [35]. The bone shape of the recuperator is a result of the need to keep the channel width narrow in order to prevent excess stress on the plates at high temperatures, due to the pressure difference between the hot and cold channels, while maintaining sufficiently large header tube diameters so as not to induce a significant pressure drop.

To enable testing at higher temperatures while simulating the different pressures within the recuperator, a throttle plate and a combustion chamber (shown in Fig. 5) were positioned between the cold-side outlet and hot-side inlet. The throttle plate had a 1.6 mm hole simulating the pressure drop that would be observed in the STBC due to the turbine and receiver, while the combustion chamber simulated the solar receiver, which increased the recuperator hot-side inlet

temperature. Also indicated in Fig. 5 are the points at which data was gathered with a combination of in-stream and weld pad K-type thermocouples as well as highly accurate pressure transducers. Each measurement location in Fig. 5 is indicated with an arrow pointing towards two threaded holes where an in-stream thermocouple and pressure transducer was installed. Five measurement locations are indicated in the figure.

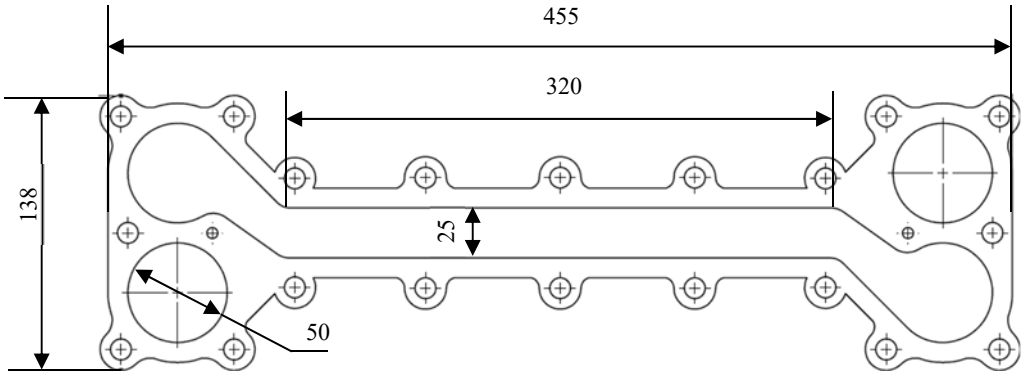


**Fig. 3.** Mark I – Recuperator channel dimensions in millimetres.

**Fig. 4.** Mark I – Experimental model being assembled with Calofer.

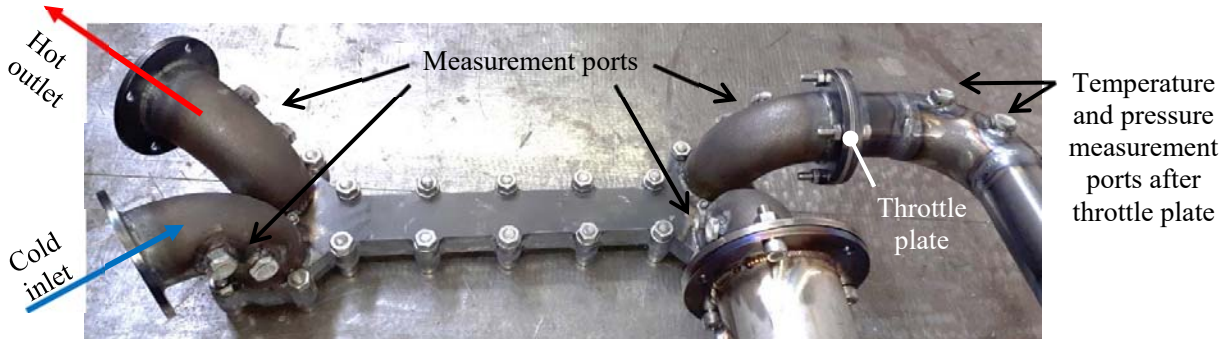


**Fig. 5.** Complete Mark I recuperator test rig.

Because the pressure transducers could not exceed 80 °C or risk failure, they had to be extended away from the measurement points by a length of copper tube so that the high temperatures at some of the positions could be cooled before reaching the pressure probes. This introduced a few

issues, chief among which was the additional heat loss, which was added to the heat loss model. Another possible issue could be that the added air volume in the tube could interfere with pressure measurement because air is compressible. However, in this work, transient data was not needed for the experimental work, and only steady-state values were used. Thus, any small undulations in pressure measurement would be negated.

The entire setup was insulated extensively with both ceramic fibre board and ceramic fibre blanket to reduce heat loss. Fig. 6 shows the placement of the recuperator core surface thermocouples as well as the thermocouples situated on the surface of the insulation. Note that the bottom recuperator surface thermocouple is located in the same position as the top surface probe.

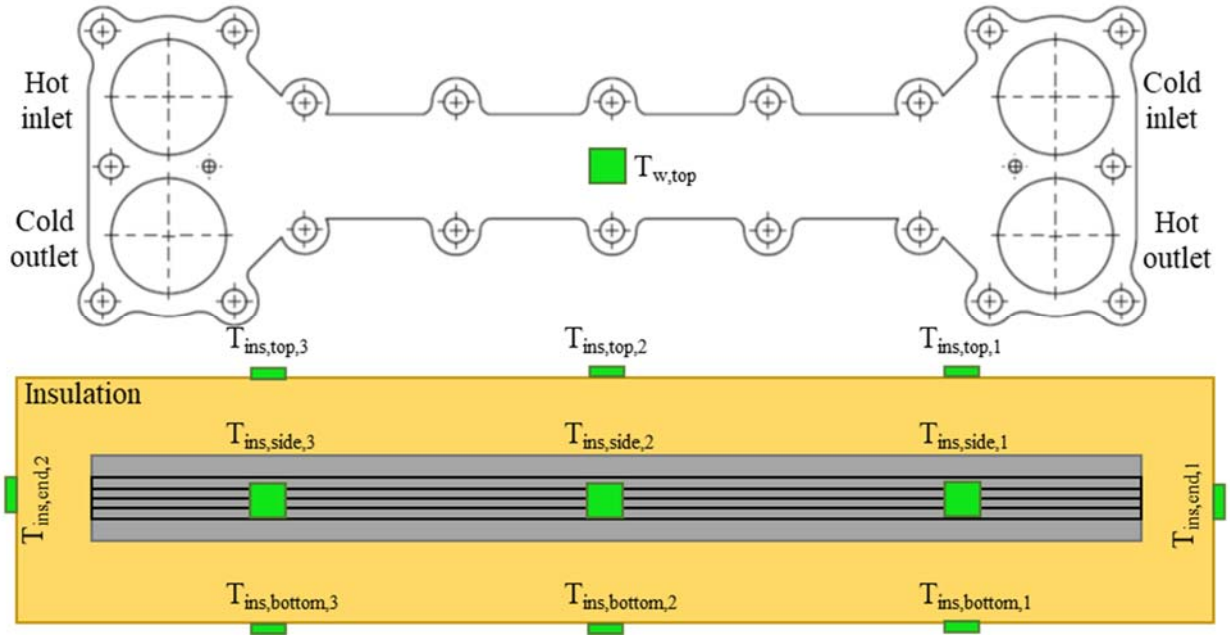


**Fig. 6.** Mark I recuperator surface and insulation thermocouple placement.

The insulation temperatures were measured at 11 points, three each on the top, side and bottom surfaces as well as one on each end of the recuperator body. The probes were placed down the centre line of the fluid path, with the first (denoted by the number 1) being closest to the cold end of the test rig, i.e. the opposite side of where the combustion chamber is situated and where the cold inlet is; the second (denoted by the number 2) in the middle, directly above the weld pad K-type thermocouple on the recuperator; and the third (denoted by the number 3) closest to the hot side where the combustion chamber is located. The remaining two probes were situated on the ends of the recuperator body, one at the air inlet and the other at the combustion chamber.

*3.2. Test 2 – Mark II rig*

The second test rig (Mark II) was constructed from grade 316 stainless steel, implementing wider and longer channels, as well as more of them (20 versus 2 channel pairs as compared with

Mark I). The goal of testing a recuperator with more channels was to increase the air mass flow rate. The need to test at higher flow rates originated from five requirements, namely to have better combustion of the LPG (see Section 4.1.4), to experiment with alternative assembly techniques, to gain a better insight into the manufacturing logistics and expenses, to explore new geometries for further validation of the theoretical model, and to implement an industry standard mass flow meter so that accurate mass flow data could be retrieved. Fig. 7 displays a gasket from the Mark II test rig.

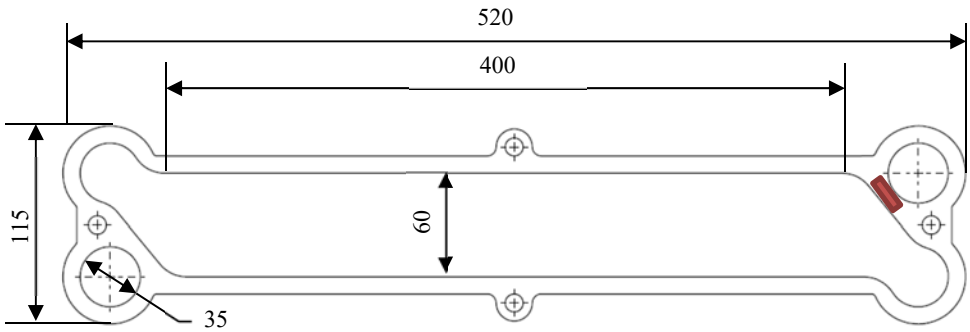


**Fig. 7.** Mark II gasket during assembly process.

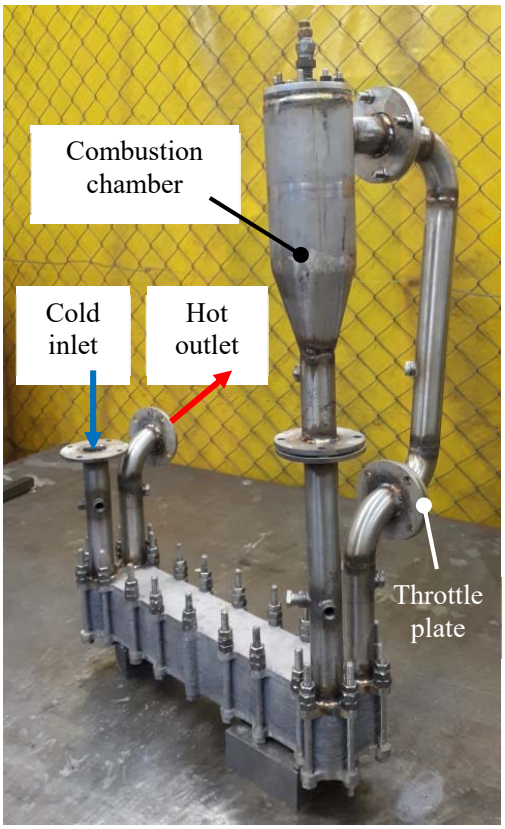


**Fig. 8.** Assembled Mark II core being positioned with the combustion chamber.

The Calofer was prepared for application by mixing 1.5 litres with 200 millilitres of water to dilute the mixture for even application and to extend the drying time. Only a portion of this mixture, roughly 500 millilitres, was actually adhered to the gaskets of the 20 channel pairs. The remainder of the Calofer was either wasted via spillage or via the cleaning of the application equipment (a small foam paint roller), or it was stored for later use.

The completely assembled Mark II recuperator core is displayed in Fig. 8. Therein, the M10, 12.8 hardness, grade 316 stainless steel cap screws used to apply the clamping force can be observed. The ports used to attach or insert the measurement probes on the header tube inlets and outlets are also visible. Similar to the Mark I rig, Mark II was then pressure tested after the initial assembly. However, unlike Mark I, Mark II showed a leak. This could be the result of the gasket geometry not being optimal for sealing as well as uneven clamping forces causing warpage and inconsistent application of the Calofer. However, the pressure test did indicate that the mass flow leak occurred from the cold channel into the hot channel via the area of the gasket separating the cold channel from the hot channel manifold port (indicated in red in Fig. 7). It was also discovered that the leak was present on the hot side of the recuperator, i.e. between the cold channel outlet and the hot channel inlet. This meant that by utilising the throttle plate mass flow data, the leak could be quantified by comparing the throttle plate mass flow data with data of the mass flow meter, which shows the mass flow rate through the core of the recuperator.

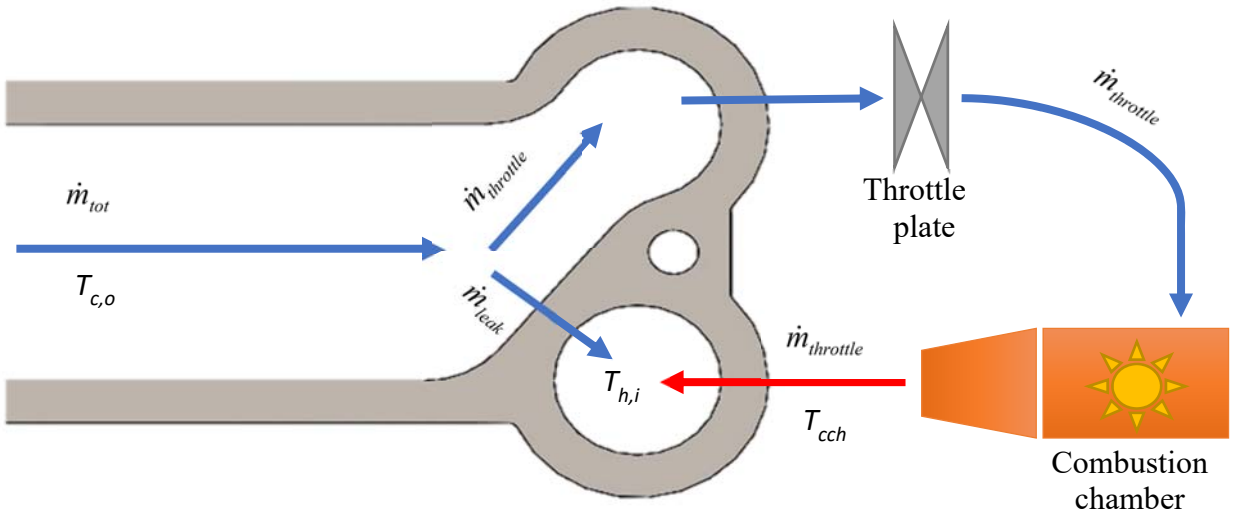


**Fig. 9.** Mark II leak and mass balance schematic.

The hot-side manifold tube leak, which was identified during the pressure test, could be quantified by means of a mass flow rate comparison as well as a mass balance if one considers a control volume around the area highlighted in Fig. 7. Fig. 9 is a schematic representation of the leak area. It details the division of the mass flow as well as which temperatures had to be considered. Fig. 10 shows the placement of in-stream thermocouples within the Mark II test rig.

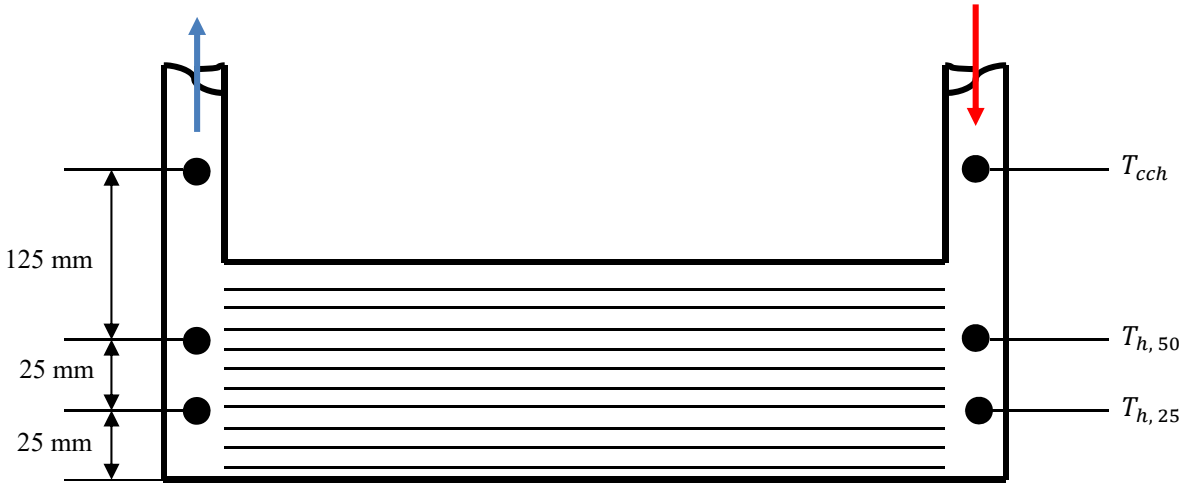


**Fig. 10.** Mark II thermocouple placement.

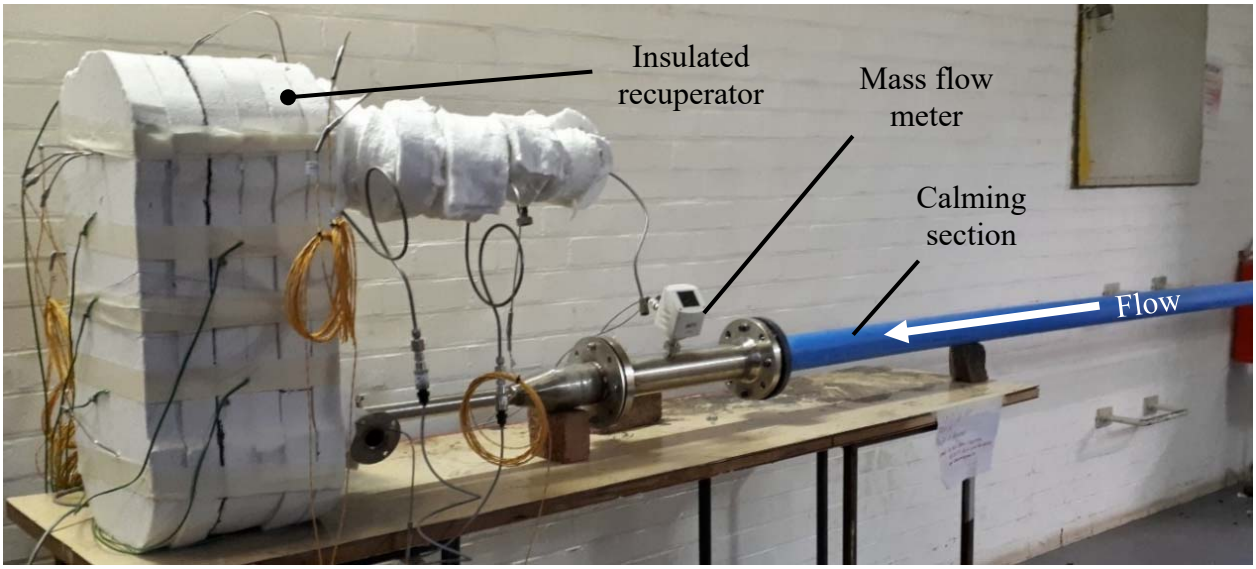


**Fig. 11.** Complete Mark II test rig with calming section and mass flow meter.

Fig. 11 depicts the completely assembled Mark II test rig with the Suto S421 mass flow meter installed. A throttle plate with a 7.1 mm hole was installed between the cold outlet tube and the combustion chamber, similar to Fig. 5. What is noteworthy is the 4 metre-long inlet section. This was installed so that fully developed, uniform flow would pass the mass flow meter, and accurate data could be collected. To mitigate the corrosion that was discovered in the Mark I test rig (see Section 4.1.4), the Mark II test rig was oriented vertically as opposed to horizontally so that any condensation formed in the hot channels upon start-up could drain from the hot outlet. The insulation thickness was also increased from 50 mm that was implemented for Test 1 to a thickness of 100 mm for Test 2, to further reduce the total heat loss.

*3.3 Measurement equipment*

Calibrated in-stream and weld-pad (surface temperature) K-type thermocouples were used. The uncertainty associated with the WIKA TC 40 in-stream thermocouples is a function of the temperature as shown in Eq. (19).

$$Uncertainty\,(T) = 0.00000327(T)^2 + 0.00069333(T) + 0.798 \quad (19)$$

For pressure measurements, calibrated Honeywell ratiometric pressure transducers with a maximum absolute operating pressure of 344.7 kPa were used. The maximum pressure transducer uncertainty was 1.66 kPa. The transducers required a supply voltage of 5 V, where 0 kPa was set at 10% (0.5 V) and 344.7 kPa at 90% (4.5 V) of 5 V. The pressure function is shown in Eq. (20).

$$P = 86.1845(V) - 43.09225 \quad (20)$$

The mass flow rate was calculated by considering both the temperature and pressure measurements on either side of the throttle plate. In doing so, the mass flow rate was determined using Mach number relations for air flow through the throttle plate hole. The calibrated Suto S421 mass flow meter was used to determine the total mass flow rate through the recuperator core. A Keysight 34972A LXI data acquisition unit was used with an accuracy of 1 °C for K-type thermocouple measurements and 0.0041% when measuring DC voltage.

## 4. Testing and results

In this section, the temperature, mass flow and pressure measurements are discussed for the Mark I and Mark II recuperators. Approximately 25 ml of the low-cost sealant was used per channel pair. The assembly cost was found to be low relative to welding or furnace brazing costs.

*4.1. Test 1*

Test 1 was carried out using the Mark I recuperator (see Section 3.1).

*4.1.1 Temperatures*

Firstly, the wall temperature measurements were compared with the in-stream temperature measurements. This was due to the in-stream thermocouple being heated to a higher temperature than the walls, resulting in radiative heat transfer (radiation effect on the in-stream thermocouples). Table 1 shows that the difference between the measured in-stream and wall temperatures in Kelvin only ranges from 0.6% to a maximum of 3.7% for the hot inlet temperature, because of the well-insulated recuperator. To calculate the effectiveness, the maximum available heat transfer needs to be found using Eq. (9). Subsequently, the heat transfer for the channel in question needs to be determined. Eq. (10) is used to determine the heat transfer from the hot channels, while Eq. (11) is used to determine the heat transfer to the cold channels.

The effectiveness values for either the hot or cold channels can be determined by substituting into Eq. (21). It must be noted that the most important effectiveness value is that of the cold channel because this effectiveness indicates how much of the waste heat is being recycled back into the cycle. Finally, the amount of heat loss that occurs to the environment can be ascertained by implementing Eq. (22).

$$\varepsilon_{[h|c]} = \frac{\dot{Q}_{[h|c]}}{\dot{Q}_{max}} \tag{21}$$

$$\dot{Q}_{loss} = \dot{Q}_h - \dot{Q}_c \tag{22}$$

**Table 1**
Averaged in-stream and wall temperature measurements at steady state (Mark I).

| | |
|---|---|
| Cold inlet temperature ($T_{c,i}$) [°C] | 48.9 |
| Cold outlet temperature ($T_{c,o}$) [°C] | 258.3 |
| Cold outlet wall temperature ($T_{c,w,o}$) [°C] | 254.9 |
| Temperature after throttle ($T_{at}$) [°C] | 218.2 |
| Wall temperature after throttle ($T_{w,at}$) [°C] | 213.7 |
| Hot inlet temperature ($T_{h,i}$) [°C] | 406.4 |
| Hot inlet wall temperature ($T_{h,w,i}$) [°C] | 382.3 |
| Hot outlet temperature ($T_{h,o}$) [°C] | 72.7 |

Table 2 shows the averaged temperatures at steady state for the surface thermocouple measurements. What is observable about the top, side and bottom surface temperatures is that they increased more exponentially than linearly over the length of the recuperator due to the fact that the conductivity of the insulation increased with temperature. A curve was fitted to the top, side and bottom surface temperatures, yielding correlation coefficients of $R^2_{top}$ = 0.8236, $R^2_{side}$ = 0.9912 and $R^2_{bottom}$ = 0.9972 for the top, side and bottom functions respectively. This yields Eqs. (23), (24) and (25):

$$T_{top}(x) = 24.14e^{0.468x} \tag{23}$$

$$T_{side}(x) = 24.78e^{0.149x} \quad (24)$$

$$T_{bottom}(x) = 25.88e^{0.381x} \quad (25)$$

Equations (23), (24) and (25) are integrated for $x$-values from 0 to 1, representing the length of the recuperator surface to give average insulation surface temperatures of $T_{ins,top,avg}$ = 30.8 °C, $T_{ins,side,avg}$ = 26.7 °C and $T_{ins,bottom,avg}$ = 31.5 °C. These average values are shown in Table 2. The measured insulation temperatures on the ends of the recuperator were taken to be the average values due to the small width relative to the length. The values in Table 2 are used for validation of the model.

**Table 2**
Recuperator steady-state averaged heat loss temperatures (Mark I).

| | | | |
|---|---|---|---|
| $T_{w,top,avg}$ [°C] | 139.4 | | |
| $T_{w,bottom,avg}$ [°C] | 142.5 | | |
| $T_{ins,top,1}$ [°C] | 25.7 | $T_{ins,top,avg}$ [°C] | 30.8 |
| $T_{ins,top,2}$ [°C] | 26.9 | | |
| $T_{ins,top,3}$ [°C] | 41 | | |
| $T_{ins,side,1}$ [°C] | 24.7 | $T_{ins,side,avg}$ [°C] | 26.7 |
| $T_{ins,side,2}$ [°C] | 26.9 | | |
| $T_{ins,side,3}$ [°C] | 28.7 | | |
| $T_{ins,bottom,1}$ [°C] | 26 | $T_{ins,bottom,avg}$ [°C] | 31.5 |
| $T_{ins,bottom,2}$ [°C] | 31 | | |
| $T_{ins,bottom,3}$ [°C] | 38.1 | | |
| $T_{ins,end,1}$ [°C] | 26.1 | | |
| $T_{ins,end,2}$ [°C] | 100.2 | | |

*4.1.2 Pressures*

The pressure measurements took place at the same locations as the in-stream thermocouples. The measurement of the pressures allows for three key pieces of information to be determined, namely the mass flow rate, which is discussed in Section 4.1.3, the pressure ratio, and the pressure losses. The atmospheric pressure for the testing was taken at the beginning and end of

each test and was found to remain constant over that period at $P_{atm}$ = 87 kPa. Thus, only four pressures were actively measured during the tests, and their steady-state averaged values can be observed in Table 3.

**Table 3**
Recuperator steady-state averaged absolute pressures (Mark I).

| Cold inlet pressure ($P_{c,i}$) [kPa] | Cold outlet pressure ($P_{c,o}$) [kPa] | Pressure after throttle ($P_{at}$) [kPa] | Hot inlet pressure ($P_{h,i}$) [kPa] |
|---|---|---|---|
| 174.1 | 173.1 | 134 | 132.5 |

The pressure ratio is calculated using Eq. (26), while Eqs. (27), (28) and (29) allow for the cold-side, hot-side and total pressure losses to be found:

$$r = \frac{P_{c,i}}{P_{atm}} \tag{26}$$

$$\Delta P_c = P_{c,i} - P_{c,o} \tag{27}$$

$$\Delta P_h = P_{h,i} - P_{atm} \tag{28}$$

$$\Delta P_{tot} = \Delta P_c + \Delta P_h \tag{29}$$

*4.1.3 Mass flow rate*

The role of the throttle plate in the experimental setup was to simulate the pressure drop that would be produced by the rest of the small-scale STBC, as well as to allow for the determination of the mass flow rate by means of compressible flow relations utilising Mach numbers. The throttle plate (orifice plate when used as a measurement device) had a hole of known diameter (1.6 mm), and the pressures and temperatures on either side of the throttle plate were measured, thus allowing the Mach number to be calculated using Eq. (30), followed by the mass flow rate using Eq. (31) [44]:

$$M = -11.343\left(\frac{P_{at}}{P_{c,o}}\right)^3 + 23.971\left(\frac{P_{at}}{P_{c,o}}\right)^2 - 18.163\left(\frac{P_{at}}{P_{c,o}}\right) + 5.5891 \tag{30}$$

$$\dot{m} = A_{throttle}\left[\frac{P_{c,o}}{\sqrt{T_{c,o}}} \cdot \sqrt{\frac{\gamma}{R}} \cdot \frac{M}{\left[1 + M^2\left(\frac{\gamma - 1}{2}\right)\right]^{\frac{\gamma+1}{2(\gamma-1)}}}\right] \tag{31}$$

where it is assumed that the gas constants, $\gamma$ = 1.4 and $R$ = 287 J/kg.K for air [36], and the temperature is in Kelvin.

*4.1.4 Results*

**Table 4**
Main experimental results (Mark I).

| | |
|---|---|
| Mass flow rate ( $\dot{m}_{tot}$ ) [kg/s] | 0.000535 |
| Maximum heat transfer rate ($\dot{Q}_{max}$) [W] | 194.2 |
| Hot-side heat transfer rate ($\dot{Q}_h$) [W] | 182.5 |
| Cold-side heat transfer rate ($\dot{Q}_c$) [W] | 113.7 |
| Total heat loss rate ($\dot{Q}_{loss}$) [W] | 68.7 |
| Cold-side effectiveness ($\varepsilon_c$) | 0.586 |
| Pressure ratio ($r$) | 2 |
| Cold-side pressure loss ($\Delta P_c$) [kPa] | 0.9 |
| Hot-side pressure loss ($\Delta P_h$) [kPa] | 45.5 |
| Total pressure loss ($\Delta P_{tot}$) [kPa] | 46.4 |

The results of the data and equations in the previous three sections are presented in Table 4 for the Mark I recuperator. What is noteworthy about the results is the relatively low effectiveness and fairly high hot-side pressure loss. To gain more insight into the reason for this occurrence as well as the performance of the high-temperature sealant and the recuperator's ability to be dismantled, the test rig was disassembled. The Soudal Calofer sealed the recuperator very well but still allowed the plates to be separated without much difficulty. Upon inspection, the cold-side channels appeared to have some surface rust, most likely due to moisture. This was to be expected because the material used was mild steel. Despite the rust, there was no fouling, which resulted in a measurable layer. However, the severity of the contamination that was discovered in the hot channels was unprecedented. A thick layer of black soot coated all the heat transfer surfaces. As a result of the incomplete combustion, the fouling layer was estimated to be anywhere between 0.2 to 0.4 mm thick on each surface. This resulted in the 1 mm channel height, $b$, being reduced to a height varying from 0.6 mm to 0.2 mm, thus explaining the substantial pressure loss. Fig. 12 provides some perspective on the contrast between the cold channels (left) and the hot channels (right).

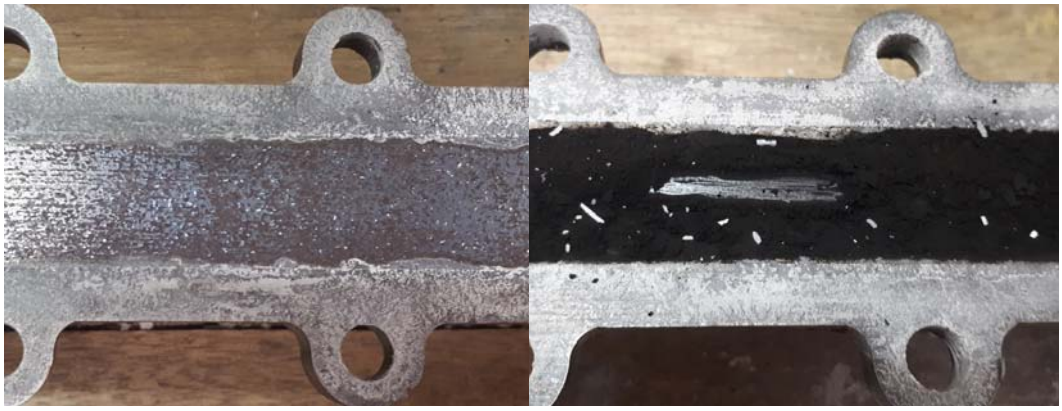

**Fig. 12.** Condition of the cold channels (left) and the hot channels

*4.1.5 Model validation*

To compare the model with the experimental results, the parameters that characterised the experimental setup during testing had to be inputted into the model, as shown in Table 5. Additional inputs that were necessary to approximate the experimental results included adding a fouling layer thickness to the hot-side geometry.

**Table 5**
Mark I theoretical model inputs.

| | |
|---|---|
| Pressure ratio ($r$) | 2 |
| Mass flow rate ($\dot{m}_{tot}$) [kg/s] | 0.000535 |
| Cold inlet temperature ($T_{c,i}$) [°C] | 48.9 |
| Hot inlet temperature ($T_{h,i}$) [°C] | 406.4 |
| Channel width ($a$) [m] | 0.025 |
| Channel height ($b$) [m] | 0.001 |
| Channel length ($L$) [m] | 0.32 |
| Plate thickness ($t$) [m] | 0.001 |
| Number of channel pairs ($N$) | 2 |

An average fouling layer thickness of $t_f$ = 0.321 mm was assumed on each surface of the hot channel, which aligned with the measured fouling thicknesses attained during the disassembly of the test rig. Additionally, the hot-side fouling factor had to be increased from the cold-side value of $R_{f,c}$ = 0.0006 m$^2$.K/W to $R_{f,h}$ = 0.0125 m$^2$.K/W, which at the determined fouling thickness corresponded to a fouling thermal conductivity of $k_f$ = 0.026 W/m.K. This conductivity is low

but within the possible range of fouling conductivities. Table 6 includes the remainder of the outputs from the model as well as a comparison with the experimental data.

**Table 6**
Mark I main model outputs and comparison.

| Component | $\dot{Q}_{loss}$ [W] | $\varepsilon_c$ (%) | $\Delta P_c$ [kPa] | $\Delta P_h$ [kPa] | $\Delta P_{tot}$ [kPa] | $T_{c,o}$ [°C] | $T_{h,o}$ [°C] |
|---|---|---|---|---|---|---|---|
| Model | 68.68 | 0.586 | 0.98 | 45.4 | 46.38 | 258.5 | 77 |
| Experimental | 68.7 | 0.586 | 0.9 | 45.5 | 46.4 | 258.3 | 72.7 |
| Difference | 0.02 | 0 | 0.08 | 0.1 | 0.02 | 0.2 | 4.3 |

The model outputs tend to adhere to the experimental data quite well. The 4.28 °C difference for the hot outlet temperature indicates that there are some minor additional experimental heat losses for which the model does not account. The areas where the model lacks with respect to estimating the heat losses can be observed in Table 7, where the heat loss temperatures calculated by the model are shown and compared with the experimental measurements. The model considers the insulation thicknesses, which are inputted values that matched the insulation thickness used on the test rig. These value are $t_{ins,top} = t_{ins,bottom} = 60$ mm , $t_{ins,side} = 77.5$ mm and $t_{ins,end} = 60$ mm for the top, bottom, side and end insulation sections respectively.

**Table 7**
Model heat loss temperatures and comparison (Mark I).

| Component | $T_{ins,top,avg}$ [°C] | $T_{ins,side,avg}$ [°C] | $T_{ins,bottom,avg}$ [°C] | $T_{ins,end,1}$ [°C] | $T_{ins,end,2}$ [°C] | $T_{w,top,avg}$ [°C] | $T_{w,bottom,avg}$ [°C] |
|---|---|---|---|---|---|---|---|
| Model | 30.6 | 27.3 | 31.2 | 27.5 | 100.16 | 159.6 | 141.4 |
| Experimental | 30.8 | 26.7 | 31.5 | 26.1 | 100.2 | 139.4 | 142.5 |
| Difference | 0.2 | 0.6 | 0.3 | 1.4 | 0.04 | 20.2 | 1.1 |

Testing showed that although the Calofer sealed the Mark I recuperator very well, the combustion chamber design was not suited to the low air flow rates. The inability for the LPG to combust stoichiometrically led to incomplete combustion occurring. This was indicated during initial testing of the chamber alone where a large yellow flame protruded from the opening, as well as during testing when black soot was occasionally ejected from the recuperator outlet. The low effectiveness is attributed to the low number of channel pairs. This results in the large heat losses incurred by the top and bottom surfaces only being distributed among a small number of channels; thus, the heat loss per channel is high, significantly reducing the effectiveness. Increasing the number of channels would therefore also increase the effectiveness, purely from a relative heat loss perspective.

*4.2. Test 2*

The Mark II recuperator was used in Test 2 (see Section 3.2).

*4.2.1 Temperatures*

**Table 8**

Test 2 steady-state fluid temperatures (Mark II).

| Cold inlet temperature ($T_{c,i}$) [°C] | Cold outlet temperature ($T_{c,o}$) [°C] | Temperature after throttle ($T_{at}$) [°C] | Combustion temperature ($T_{cch}$) [°C] | Hot inlet temperature ($T_{h,i}$) [°C] | Hot outlet temperature ($T_{h,o}$) [°C] |
|---|---|---|---|---|---|
| 22.40 | 479.79 | 472.68 | 769.36 | 566.38 | 139.48 |

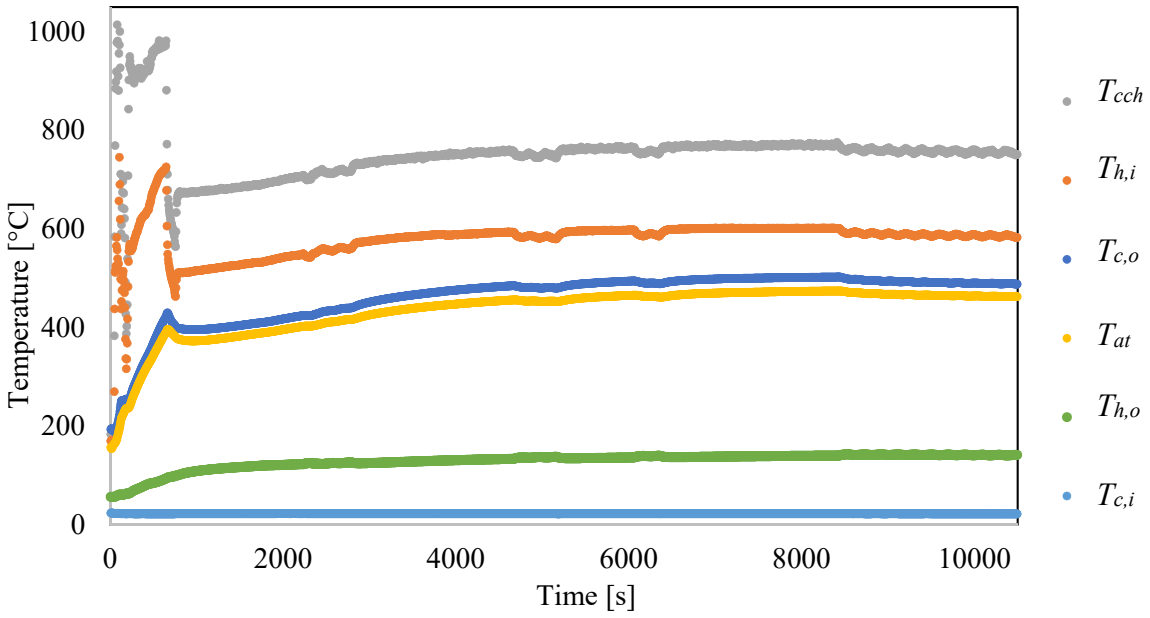


**Fig. 13.** Test 2 measured thermocouple temperatures versus time.

Test 2 exhibited an initial period of heavy transience while the combustion chamber was being calibrated to maintain a uniform temperature. Once stabilised, a steady-state region of operation was observed from 7100 seconds to 8520 seconds. Fig. 13 displays the temperature data for the fluid stream at the various points of measurement. One of the advantages of the Mark II test rig over the Mark I setup was that there were more in-stream thermocouples to measure fluid temperature at various points. The steady-state averaged fluid temperatures for Test 2 are shown in Table 8. The noteworthy difference between the combustion temperature and the hot inlet temperature is discussed in Section 4.2.3.

*4.2.2 Pressures*

The steady-state pressure data for Test 2 is listed in Table 9. The pressure data gathered was consistent, and the cold inlet pressure was the parameter that was maintained at a constant value

throughout the testing to achieve a pressure ratio of about 1.5, which was proposed for the small-scale STBC [11].

**Table 9**
Test 2 steady-state absolute pressure values.

| Atmospheric pressure ($P_{atm}$) [kPa] | Cold inlet pressure ($P_{c,i}$) [kPa] | Cold outlet pressure ($P_{c,o}$) [kPa] | Pressure after throttle ($P_{at}$) [kPa] | Hot inlet pressure ($P_{h,i}$) [kPa] |
|---|---|---|---|---|
| 87.93 | 130.85 | 127.89 | 113.31 | 111.90 |

*4.2.3 Mass flow rate*

**Table 10**
Test 2 mass flow data.

| Total mass flow rate ($\dot{m}_{tot}$) [kg/s] | Throttle mass flow rate ($\dot{m}_{throttle}$) [kg/s] | Leak mass flow rate ($\dot{m}_{leak}$) [kg/s] |
|---|---|---|
| 0.0147 | 0.00499 | 0.0097 |

**Table 11**
Test 2 calculated hot inlet temperature.

| Calculated hot inlet temperature ($T_{h,i}$) [°C] | Averaged hot inlet manifold temperature ($T_{h,i\_avg}$) [°C] |
|---|---|
| 576.95 | 566.38 |

$$h_{h,i} = \frac{\dot{m}_{leak} \cdot h_{c,o} + \dot{m}_{throttle} \cdot h_{cch}}{\dot{m}_{tot}} \tag{32}$$

The total mass flow rate of air through the recuperator core was provided by the mass flow meter, while the throttle mass flow rate was provided via the same methodology implemented in Section 4.1.3, specifically Eqs. (30) and (31). The leak amount as determined via the experimental data was simply the difference between the aforementioned mass flow rates. Note that the leak only affected the hot inlet temperature of the recuperator core, which still experienced the full mass flow rate. Table 10 contains the mass flow rates used to calculate the hot inlet temperature. Using Eq. (32) as well as the enthalpy values of the fluid streams, the hot inlet enthalpy can be determined. Once the hot inlet enthalpy is calculated, it can be used to find the hot inlet temperature from thermodynamic tables [44], the result of which is represented in Table 11. The hot inlet temperature to be calculated can be compared with the average of the manifold temperature measurements, $T_{h,25}$ and $T_{h,50}$ (see Fig. 10). The calculated hot inlet temperature is relatively close

to the average of the manifold fluid temperatures, exceeding the measured value slightly. Therefore, the calculated hot fluid inlet temperature confirms the leak mass flow rate.

*4.2.4 Results and validation*

**Table 12**
Mark II theoretical model inputs.

| | |
|---|---|
| Pressure ratio ($r$) | 1.49 |
| Mass flow rate ($\dot{m}_{tot}$) [kg/s] | 0.0147 |
| Cold inlet temperature ($T_{c,i}$) [°C] | 22.4 |
| Hot inlet temperature ($T_{h,i}$) [°C] | 577 |
| Channel width ($a$) [m] | 0.06 |
| Channel height ($b$) [m] | 0.0009 |
| Channel length ($L$) [m] | 0.4 |
| Plate thickness ($t$) [m] | 0.0009 |
| Number of channel pairs ($N$) | 20 |

To conduct a validation, the Mark II recuperator geometries and Test 2 fluid conditions are entered into the model for the recuperator core. Table 12 contains all the necessary inputs to analyse and compare the theoretically calculated performance with the experimental results. Because of the accurate mass flow rate measurements, the calculated hot inlet temperature was utilised for the effectiveness calculation. Table 13 shows the results from the model as well as the comparison with the experimental results. The experimental results yielded a cold-side effectiveness of 82.5% and a total pressure loss of 24.9 kPa. An error propagation analysis was performed in Appendix A, which shows that an uncertainty of 0.74% and 3.32 kPa is applicable for the cold-side effectiveness and total pressure loss respectively. Upon analysis of the results, it can be noted that the model accurately predicted the cold outlet temperature, the effectiveness and the hot-side pressure loss values. The heat loss rate shows some deviation from the experimental data. However, because the calculated overall heat loss rate was a relatively low value (less than 100 W) and the thermocouples each had an error which could cascade during the calculation process, this deviation was inconsequential. The cascading of errors and additional heat loss also caused the hot outlet temperature to be experimentally higher than that of the model, while the slightly larger cold-side pressure loss was due to the leak since the cold flow channels were at a higher pressure than the hot flow channels.

**Table 13**
Mark II main model outputs, experimental results and comparison.

| Component | Model | Experimental | Difference |
|---|---|---|---|
| Total heat loss rate ($\dot{Q}_{loss}$) [W] | 64.4 | -147.9 | 212.3 |
| Cold-side effectiveness ($\varepsilon_c$) | 0.868 | 0.825 | 0.043 |
| Cold-side pressure loss ($\Delta P_c$) [kPa] | 2.08 | 2.95 | 0.87 |
| Hot-side pressure loss ($\Delta P_h$) [kPa] | 21.3 | 21.9 | 0.6 |
| Total pressure loss ($\Delta P_{tot}$) [kPa] | 23.4 | 24.9 | 1.5 |
| Cold outlet temperature ($T_{c,o}$) [°C] | 503.8 | 479.8 | 24 |
| Hot outlet temperature ($T_{h,o}$) [°C] | 99.1 | 139.5 | 40.4 |

## 5. Case study

The validated recuperator model can be used to explore the application of the recuperator within a small-scale STBC optimised by Le Roux et al. [13] using the method of entropy generation minimisation, thus providing input criteria. This process should provide some insight into the potential performance of the proposed recuperator and how changing various aspects of the available geometries affects its capabilities. The input parameters taken from Le Roux et al. [13] are displayed in Table 14.

**Table 14**
Optimised STBC input parameters.

| Pressure ratio ($r$) | Mass flow rate ($\dot{m}$) [kg/s] | Cold inlet temperature ($T_{c,i}$) [°C] | Hot inlet temperature ($T_{h,i}$) [°C] | Ambient temperature ($T_\infty$) [°C] |
|---|---|---|---|---|
| 1.49 | 0.06 | 83.7 | 726.9 | 27 |

The additional parameters that were fixed for the modelling process can be observed in Table 15. These include the plate thickness and channel height. They were fixed at this value because it is a commonly available thickness of grade 316 stainless steel sheet, from which the symmetrical plates and gaskets could easily and cost-effectively be manufactured. Therefore, the channel width could be ascertained next in a pre-calculation, using the model, to determine a fixed channel width input for the remainder of the modelling. This was achieved by increasing the width of the channel so that a pressure ratio of $r$ = 2 (selected as a precaution to account for possible off-optimal operating points during transient periods) resulted in a safety factor of 2 between the plate stress and yield stress of grade 316 stainless steel at 800 °C. This ensured that

no significant deflection would occur so as to close off the channels, as well as limiting creep deterioration. It was further assumed that for the real application, the LPG or another preferred fuel would be completely combusted, thus resulting in either no or an insignificant fouling layer thickness and a much lower fouling factor.

**Table 15.** Additional STBC modelling parameters.

| Plate thickness ($t$) [m] | Channel height ($b$) [m] | Channel width ($a$) [m] |
|---|---|---|
| 0.001 | 0.001 | 0.05 |

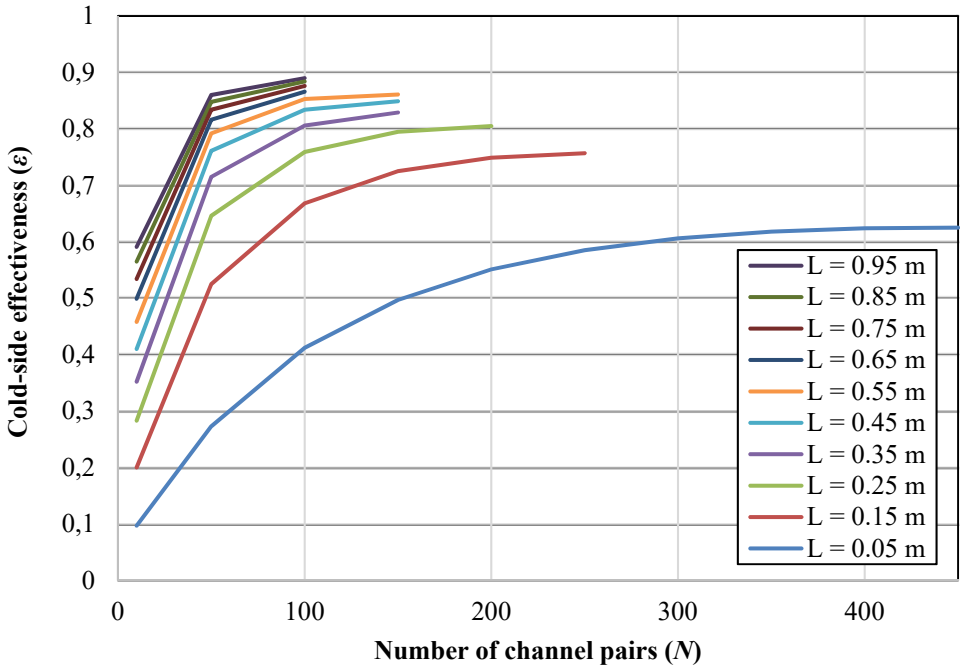


**Fig. 14.** Model results for effectiveness versus number of channel pairs at various channel lengths.

In addition to the aforementioned inputs, the same insulation thicknesses as the test rigs were used. The type and number of measurement probes that were considered in the validation were also kept consistent and matched the experimental test rig. A manifold tube diameter of 50 mm was used. Making use of these parameters, Fig. 14 and Fig. 15 were generated by plotting the cold-side effectiveness and total pressure loss against the number of channels for varying channel lengths respectively. Additionally, the plots for the various channel lengths ended at different positions due to the hot-side outlet temperature approaching the cold-side inlet temperature. Increasing the number of channels from this point on would only result in no further useful heat transfer occurring.

Another geometrical factor that was explored was that of the manifold tube diameters. The channel length was kept constant at $L$ = 0.25 m at four different manifold tube diameters. The

smallest manifold tube diameter was 25 mm because any smaller produced larger pressure losses than what could possibly be allowed. The largest manifold tube diameter was 100 mm because increasing it further would not result in any significant reduction in pressure loss, but would continue to increase the heat loss, resulting in a lower effectiveness. Fig. 16 and Fig. 17 show the results of the aforementioned analysis.

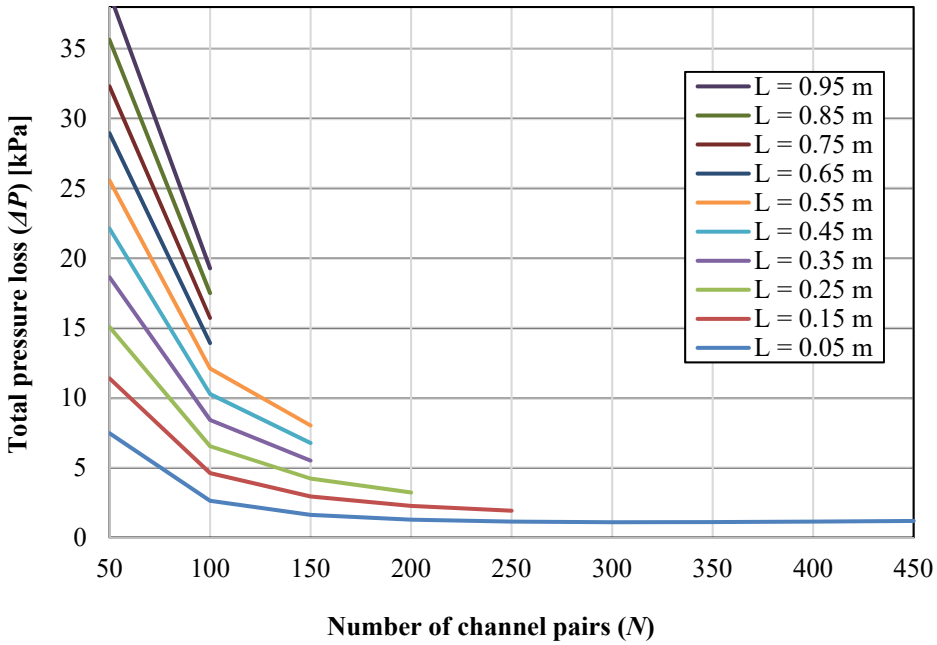


**Fig. 15.** Model results for pressure loss versus number of channel pairs at various channel lengths.

The results of the analyses demonstrated that there appeared to be no combination of geometries which allowed the recuperator design with parameters shown in Tables 14 and 15 to adhere to the specifications set forth by McDonald [22], because an effectiveness of 90% or above could not be achieved while maintaining a pressure loss of below 5%. A 5% pressure loss with the pressure ratio stipulated in Table 14 at an atmospheric pressure of $P_{atm}$ = 87 kPa equates to a pressure loss of $\Delta P_{tot}$ = 6.5 kPa. Fig. 15 shows that this can be achieved when $N$ = 150 and $L$ = 0.45 m, with an effectiveness of about 85%. A maximum cold-side effectiveness of 89% with a total pressure loss of 19 kPa can be obtained when $L$ = 0.95 m, as shown in Fig. 14 and Fig. 15.

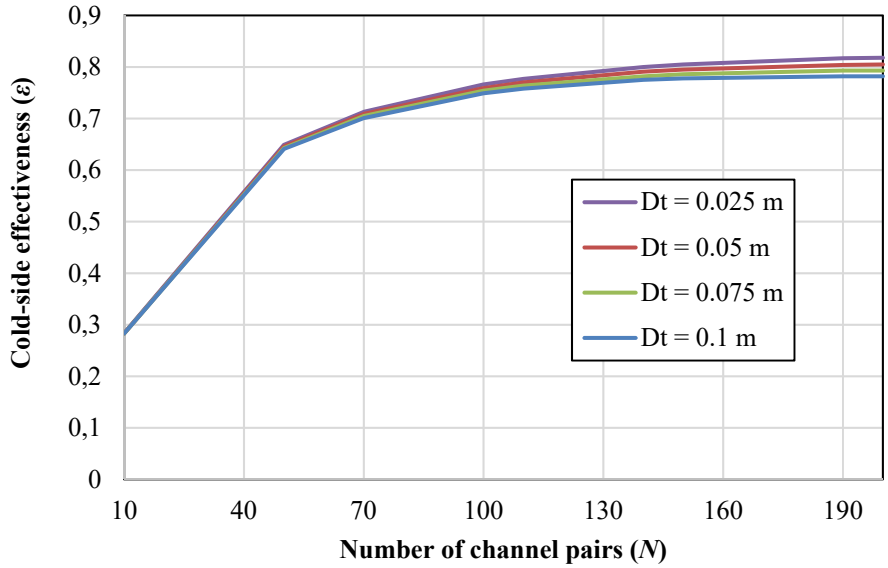


**Fig. 16.** Effectiveness versus number of channel pairs for varying manifold tube diameters.

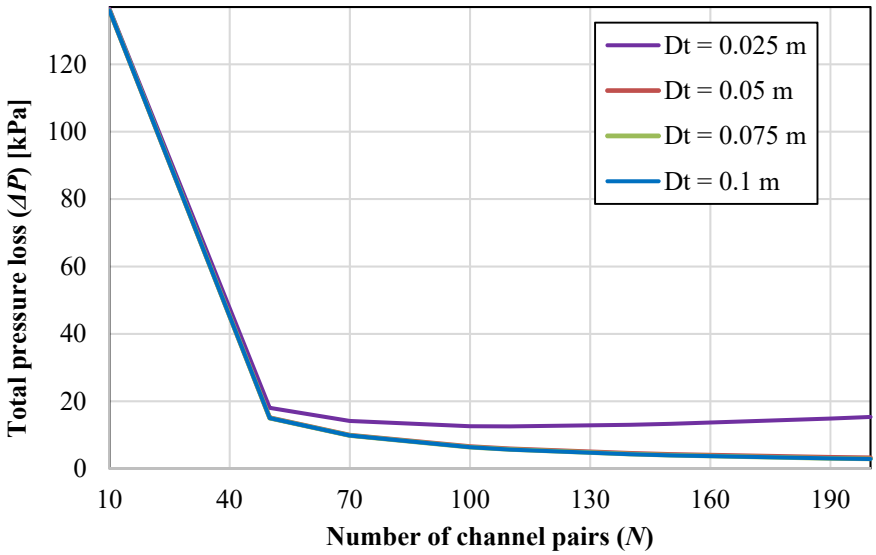


**Fig. 17.** Pressure loss versus number of channel pairs for varying manifold tube diameters.

A recuperator with $L$ = 0.95 m and $N$ = 50 is further investigated in Figs. 18, 19 and 20, with manifold tube diameter of $D_t$ = 0.0833 m. The results show that the cold-side effectiveness increases as the channel width increases and that the channel width can be chosen for minimum pressure loss. The results show that a recuperator with $L$ = 0.95 m, $N$ = 50, $a$ = 0.225 m and $b$ = 2.25 mm should allow for a cold-side effectiveness of 90% with a total pressure loss of 0.76 kPa. This result adheres to the specifications set forth by McDonald [22]. This result also correlates well with the results shown in Le Roux and Sciacovelli [18] where an optimum recuperator geometry of $L$ = 1.5 m, $N$ = 45, $a$ = 0.225 m and $b$ = 2.25 mm was found for a solar Brayton cycle with a net power output of 2.05 kW, a total mass flow rate of 0.05 kg/s and a

thermal storage temperature of 1100 K. It should be noted from Fig. 20, however, that the maximum stress in the recuperator plates increases as the channel width increases, according to Eq. (17). The maximum deflection also increases with the channel width according to Eq. (18). Fig. 20 shows that by increasing the wall thickness, the maximum stress and deflection can be decreased; however, the total weight and cost also increases. It is therefore recommended that, to prevent channel deflection when using wider flow channels, the implementation of a spacer in the middle of each channel can be investigated in future work, to achieve efficiencies of above 90%.

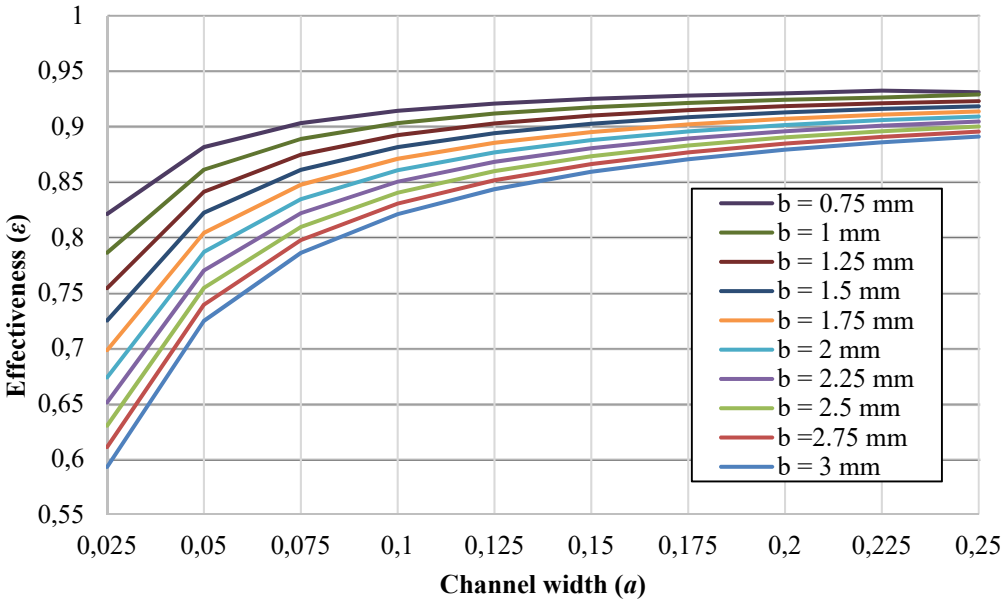


**Fig. 18.** Effectiveness versus channel width for $L = 0.95$ m, $N = 50$.

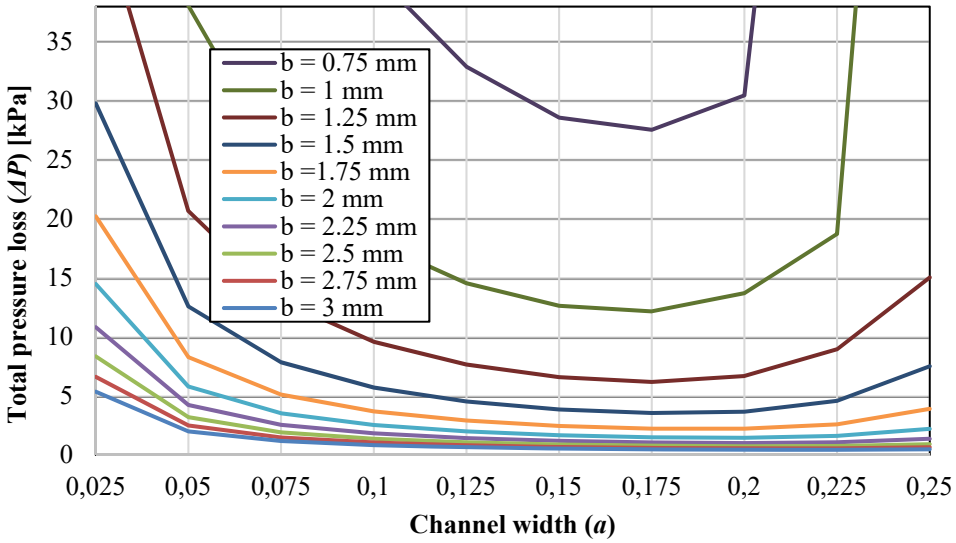


**Fig. 19.** Pressure loss versus channel width for $L = 0.95$ m, $N = 50$.

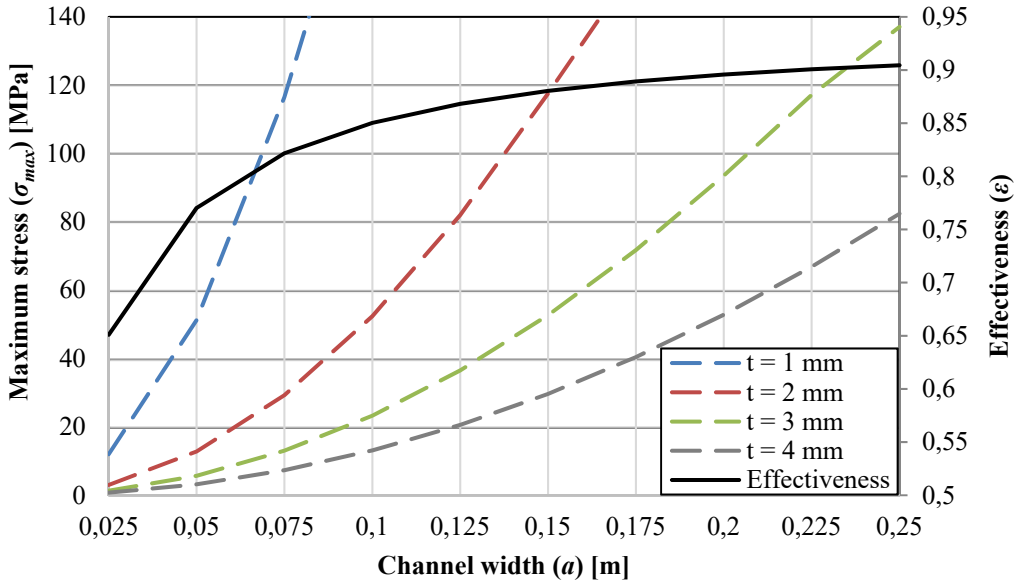


**Fig. 20.** Maximum stress and cold-channel effectiveness for $L = 0.95$ m, $N = 50$ and $b = 2.25$ mm.

## 6. Conclusion

It has been stated that a personalised micro-turbine power generation system may become as commonplace as a personal computer. Couple this to an excellent solar direct normal irradiation (DNI) resource, and a small-scale recuperated solar thermal Brayton cycle (STBC) shows enormous potential. A recuperator comprises up to 30% of the capital cost associated with a micro-turbine package. Thus, the objective of this research was to investigate a metal gasket in a clamped plate-type recuperator, together with a low-cost high-temperature sodium silicate-based sealant, that can be cost-effectively manufactured. The effectiveness and pressure drop characteristics of the clamped plate-style recuperator were considered. Two experimental investigations were performed on two different small-scale test rigs to validate a mathematical model, based on a novel bone-shape recuperator as well as a wide-channel recuperator. The mathematical model was used to analyse the performance of a full-scale recuperator for operation in an STBC by taking the stress and deflection of the plates into consideration.

The experimental testing showed firstly that the physical construction was simple and cost-effective, and that the clamped plate-style high-temperature sealant combination worked very well together for the recuperator core, facilitating an easy assembly and disassembly process. About 25 ml of the sealant was used per channel pair. The assembly cost was found to be low compared to the cost of welding or furnace brazing. The ability of the recuperator to be easily disassembled allowed for a thorough post-testing inspection. The construction sustained an airtight seal (Mark I) at various pressures and high temperatures for the entire testing period, provided the assembly process was done in an expedient manner as well as uniformly. Despite the occurrence of heavy soot-based fouling deposits during Test 1 due to incomplete combustion of the LPG as a result of the very low air mass flow rates, the model was able to match the values

gathered from the testing. The data showed a cold-side effectiveness of 58.6% and a total pressure loss of 46.4 kPa. In the case of Test 2, a leak of the total mass flow rate from the cold channel to the hot inlet manifold tube was identified, quantified and accounted for, after which the model closely matched the experimental results for the recuperator core. This resulted in a cold-side effectiveness of 82.5% and a total pressure loss of 24.9 kPa at an average mass flow rate of about 0.74 g/s per channel.

As a case study, input data from literature, gathered from an optimisation study conducted on a small-scale STBC, was implemented to investigate whether a specific recuperator design could function well within the STBC. The results showed that, for a total mass flow rate of 0.06 kg/s, the combination of an effectiveness of 85% and a pressure loss of 5% could be attained if 150 channel pairs with a channel height of 1 mm, a channel width of 50 mm, and a channel length of 450 mm are used. Alternatively, a cold-side effectiveness of 89% could be achieved by increasing the total pressure loss to 19 kPa with a channel length of 950 mm. The results also showed that the total pressure loss can be decreased by increasing the channel width. A cold-side effectiveness of 90% with a total pressure loss of 0.76 kPa can be attained if 50 channel pairs with a channel height of 2.25 mm, a channel width of 225 mm, and a channel length of 950 mm are used; however, the maximum stress and deflection will increase significantly. The implementation of a spacer in the middle of each channel would therefore be required.

For future work, it is recommended that a large-scale recuperator be built and tested to confirm the performance characteristics of larger mass flow rates. Furthermore, the design could possibly benefit from the addition of heat transfer enhancement mechanisms. One such adjustment would be to have the plates either laser cut and then indented to form structural ridges or to have them stamped out of sheet with the structural geometries included. This will allow for a larger channel width to be explored before mechanical stress and deflection of the plates become an issue. The main areas of concern should be the gasket geometry and assembly method so as to develop a uniform and consistent assembly technique that results in an airtight seal for every unit assembled. This may be achieved by regulating the amount of water added to the Soudal Calofer for thinning purposes to achieve a consistency which facilitates uniform application and extended drying time to allow for the assembly to be completed while not thinning the sealant too much so as to lead to a seal failure. In conjunction, the clamping force distribution is critical to sealing the inner channel division, where the leak occurred in Test 2. Alternatively, the channel division section of the gasket should be designed more carefully to aid the Calofer in sealing, perhaps by incorporating a double-walled design, thus trapping Calofer more securely. Furthermore, it is recommended that the usable lifespan of such a recuperator be determined. To do so, one or several recuperators, potentially of varying geometries, should be tested at a multitude of operating conditions. Most crucially, thermal and pressure cycling must be investigated, especially when seal integrity is concerned.

**Acknowledgements**
This work is based on the research supported by the National Research Foundation (NRF) of South Africa (Grant Number 109311), the Technology Innovation Agency of South Africa (TIA) and the University of Pretoria's Research and Development Plan (RDP). Opinions expressed, and conclusions arrived at are those of the author and are not necessarily to be attributed to the NRF, TIA or RDP.

## Appendix A. Error propagation analysis for effectiveness and pressure drop

To analyse the effect that error propagation has on the cold-side effectiveness value, which was experimentally determined for Test 2, Eq. (A-1) is considered.

$$\varepsilon_c = \frac{\dot{Q}_c}{\dot{Q}_{max}} = \frac{\dot{m}_{tot} C_{p,c} (T_{c,o} - T_{c,i})}{\dot{m}_{tot} C_{p,c} (T_{h,i} - T_{c,i})} = \frac{T_{c,o} - T_{c,i}}{T_{h,i} - T_{c,i}} \tag{A-1}$$

The effect of the combined thermocouple and data logger uncertainties can be determined for each temperature.

$$\delta T_{c,i} = \sqrt{(0.82)^2 + (1)^2} = 1.29\ °C \tag{A-2}$$

$$\delta T_{c,o} = \sqrt{(1.88)^2 + (1)^2} = 2.13\ °C \tag{A-3}$$

$$\delta T_{h,i} = \sqrt{(2.29)^2 + (1)^2} = 2.5\ °C \tag{A-4}$$

Utilising the combined uncertainties for each temperature, the uncertainty due to temperature difference can be found as shown below.

$$\delta (T_{c,o} - T_{c,i}) = \sqrt{(2.13)^2 + (1.29)^2} = 2.49\ °C \tag{A-5}$$

$$\delta (T_{h,i} - T_{c,i}) = \sqrt{(2.5)^2 + (1.29)^2} = 2.81\ °C \tag{A-6}$$

$$T_{c,o} - T_{c,i} = 479.8 - 22.4 = 457.4\ °C \tag{A-7}$$

$$T_{h,i} - T_{c,i} = 577 - 22.4 = 554.6\ °C \tag{A-8}$$

The total uncertainty associated with the cold-side effectiveness can be determined as shown below.

$$\frac{\delta \varepsilon}{|\varepsilon|} = \sqrt{\left(\frac{2.49}{457.4}\right)^2 + \left(\frac{2.81}{554.6}\right)^2} = \pm 0.74\ \% \tag{A-9}$$

The total pressure loss can be characterised by Eq. (A-10).

$$\Delta P_{tot} = \left(P_{c,o} - P_{c,i}\right) + \left(P_{h,i} - P_{h,o}\right) \tag{A-10}$$

Because of the small uncertainty in DC voltage measurement of the data acquisition unit (Keysight 34972A LXI), it will be omitted from the uncertainty analysis. Therefore, the only uncertainty which plays a role in the cascading uncertainty is the pressure transducer uncertainty. The following equations detail the calculation of the uncertainty associated with the total pressure loss.

$$\delta(P_{c,o} - P_{c,i}) = \sqrt{(1.66)^2 + (1.66)^2} = 2.35\ kPa \quad \text{(A-11)}$$

$$\delta(P_{h,i} - P_{h,o}) = \sqrt{(1.66)^2 + (1.66)^2} = 2.35\ kPa \quad \text{(A-12)}$$

$$\delta(\Delta P_{tot}) = \sqrt{(2.35)^2 + (2.35)^2} = \pm 3.32\ kPa \quad \text{(A-13)}$$

**Nomenclature**

| | |
|---|---|
| $A$ | Area, $m^2$ |
| $a$ | Channel width, m |
| $b$ | Channel height, m |
| $c$ | Capacity ratio |
| $C_p$ | Specific heat, J/kg.K |
| $D$ | Diameter, m |
| $D_h$ | Hydraulic diameter, m |
| $D_t$ | Manifold tube diameter, m |
| $E$ | Young's modulus, GPa |
| $f$ | Friction factor |
| $h$ | Enthalpy, J/kg |
| $k$ | Conductivity, W/m.°C |
| $L$ | Length, m |
| $M$ | Mach number |
| $\dot{m}$ | Mass flow rate, kg/s |
| $N$ | Number of channel pair |
| Nu | Nusselt number |
| $P$ | Pressure, Pa |
| $\dot{Q}$ | Heat transfer rate, W |
| $\dot{Q}*$ | Available solar power, W |
| $r$ | Pressure ratio |
| $R$ | Gas constant, J/kg.K |
| $R_f$ | Fouling factor, $m^2$.°C/W |
| $t$ | Thickness, m |
| $T$ | Temperature, °C |
| $U$ | Overall heat transfer coefficient, W/$m^2$.°C |
| $V$ | Velocity, m/s |

| | |
|---|---|
| $\dot{W}$ | Power, W |
| $x$ | Distance, m |
| $X$ | Dimensionless position |
| $y$ | Deflection, m |

*Greek letters*

| | |
|---|---|
| $\gamma$ | Gas constant, |
| $\varepsilon$ | Effectiveness |
| $\rho$ | Density, kg/m$^3$ |
| $\sigma$ | Mechanical stress, Pa |
| $\theta$ | Dimensionless temperature difference |

*Subscripts*

| | |
|---|---|
| *25* | Depth of 25 mm |
| *50* | Depth of 50 mm |
| *at* | After throttle |
| *atm* | Atmospheric |
| *avg* | Average |
| *bottom* | Bottom of |
| *c* | Compressor (only in Fig. 1) |
| *c* | Cold |
| *cch* | Combustion chamber exhaust |
| *channel* | Per channel |
| *end* | The end of the body |
| *f* | Fouling layer |
| *h* | Hot |
| *headertube* | Associated with the header tube |
| *i* | Inlet |
| *ins* | Insulation |
| *leak* | Denotes the leak value |
| *loss* | Loss of |
| *max* | Maximum |
| *net* | Net |
| *o* | Outlet |
| *s* | Surface |
| *side* | Side of |
| *steel* | For steel |
| *t* | Turbine |
| *throttle* | Associated with the throttle plate |
| *top* | Top of |

| | |
|---|---|
| *tot* | Total |
| *ts* | Top surface |
| *tubes* | Per tube |
| *w* | Wall |
| ∞ | Environment |

*Abbreviations*

| | |
|---|---|
| *CSP* | Concentrated solar power |
| *LPG* | Liquified petroleum gas |
| *NTU* | Number of transfer units |
| *PV* | Photovoltaic |
| *STBC* | Solar thermal Brayton cycle |

**References**


[1] N. Yakah, Heat Exchanger Design for a Solar Gas-Turbine Power Plant. Stockholm: Division of Heat and Power, KTH School of Industrial Engineering and Management, (2012).

[2] R. Korzynietz, et al., Solugas – Comprehensive analysis of the solar hybrid Brayton plant, Sol. Energy, 135 (2016) 578-589.

[3] K. Wang, et al., Experimental study on a coiled tube solar receiver under variable solar radiation condition, Sol. Energy 122 (2015) 1080-1090.

[4] M. Lanchi, et al., Investigation into the coupling of micro gas turbines with CSP technology: OMSoP project, Energy Procedia 69 (2015) 1317-1326.

[5] C.F. McDonald, C. Rodgers, The ubiquitous personal turbine - a power vision for the 21st Century, J. Eng. Gas Turb. Power 124 (2002) 835-844.

[6] D. Mills, Advances in solar thermal electricity technology, Sol. Energy 76 (2004) 9-31.

[7] A. Pietsch, D.J. Brandes, Advanced solar Brayton space power systems, In: Proceedings of the Intersociety Energy Conversion Engineering Conference (IECEC), Los Alamitos, CA (1989) 911-916.

[8] B. Dickey, Test results from a concentrated solar micro-turbine Brayton cycle integration, Vancouver, British Columbia, Canada, ASME Paper No. GT2011-45918 (2011).

[9] T. Stevens, F. Verplaetsen, M. Baelmans, Requirements for recuperators in micro gas turbines, In: Proceedings of the 4th International Workshop on Micro and Nanotechnology for Power Generation and Energy Conversion Applications, Kyoto, Japan (2004) 96-99.

[10] W.G. Le Roux, J.P. Meyer, Small-scale dish-mounted solar thermal Brayton cycle, In: Clean Energy for Sustainable Development, Queensland: Elsevier (2017) 167-190.

[11] W.G. Le Roux, Thermodynamic optimisation and experimental collector of a dish-mounted small-scale solar thermal Brayton cycle, Thesis: Pretoria, University of Pretoria (2015).

[12] T.M. Wolff, W.G. Le Roux, J.P. Meyer, Heat loss analysis for an open-cavity tubular solar receiver, Beijing, China, In: Proceedings of the 16th International Heat Transfer Conference (IHTC-16) (2018) 7695-7702.
[13] W.G. Le Roux, J.P. Meyer, Modelling the small-scale dish-mounted solar thermal Brayton cycle. SolarPACES2015 (pp. 060002-1–060002-8). Cape Town: AIP Conference Proceedings 1743 (2015).
[14] W.P.J. Visser, S.A. Shakariyants, M. Oostveen, Development of a 3 kW microturbine for CHP applications, J. Eng. Gas Turb. Power 133 (2011) 042301-1-042301-8.
[15] R.K. Shah, Compact heat exchangers for micro-turbines, Retrieved: 11 June, 2017, Available at: https://www.cso.nato.int/pubs/rdp.asp?RDP=RTO-EN-AVT-131, (2005).
[16] K.G. Allen, Performance characteristics of packed bed thermal energy storage for solar thermal power plants, Thesis: University of Stellenbosch (2010).
[17] H.M. Cameron, L.A. Mueller, D. Namkoong, Preliminary design of a solar heat receiver for a Brayton-cycle space power system, Report NASA TM X-2552, Lewis Research Centre, (1972).
[18] W.G. Le Roux, A. Sciacovelli, Recuperated solar-dish Brayton cycle using turbocharger and short-term thermal storage, Sol. Energy 194 (2019) 569-580.
[19] W.G. Le Roux, Feasibility study of a hybrid small-scale dish-mounted solar thermal Brayton cycle with cogeneration, Beijing, China, IHTC (2018) 7929-7936.
[20] C.F. McDonald, C. Rodgers, The ubiquitous personal turbine – a power vision for the 21st century, J. Eng. Gas Turb. Power 124 (2002) 835-844.
[21] D. Aquaro, M. Pieve, High temperature heat exchangers for power plants: performance of advanced metallic recuperators, Appl. Therm. Eng. 27 (2007) 389-400.
[22] C.F. McDonald, Low-cost compact primary surface recuperator concept for micro-turbines, Appl. Therm. Eng. 20 (2000) 471-497.
[23] G. Xiao, et al., Recuperators for micro gas turbines: a review, Appl. Energy 197 (2017) 83-99.
[24] A. Clay, G.D. Tansley, Exploration of a simple, low cost, micro gas turbine recuperator solution for a domestic combined heat and power unit, Appl. Therm. Eng. 31 (2011) 2676-2684.
[25] C.F. McDonald, Recuperator considerations for future higher efficiency micro-turbines, Appl. Therm. Eng. 23 (2003) 1463-1487.
[26] C. Scaccia, B. Theoclitus, Heat exchangers – types, performance and applications, Chem. Eng. 20 (1980) 121-132.
[27] T. Paanu, P. Aho, J. Ekman, H. Saveljeff, H., and Niemi, S., Effect of the exhaust gas side fouling on the performance of a plate and shell type heat exchanger, In: Proceedings of the University of Vaasa. Reports 197, (2015).
[28] J. Kesseli, K. Wolf, J. Nash, S. Freedman, Micro, industrial and advanced gas turbines employing recuperators, New York, ASME Paper No. GT2003-38938 (2003).

[29] J.L. Cordova, J.F. Walton, H. Heshmat, High effectiveness, low pressure drop recuperator for high speed and power oil-free turbogenerator, Montréal, Canada, ASME Paper No. GT2015-43718 (2015).
[30] B. Tsai, Y.L. Wang, A novel Swiss-Roll recuperator for the microturbine engine, Appl. Therm. Eng. 29 (2009) 216-223.
[31] H. Shih, Y. Huang, Thermal design and model analysis of the Swiss-roll recuperator for an innovative micro gas turbine, Appl. Therm. Eng. 29 (2009) 1493-1499.
[32] M.M. Ohadi, S.G. Buckley, High temperature heat exchangers and microscale combustion systems: applications to thermal system miniaturization, Exp. Therm. Fluid Sci. 25 (2001) 207-217.
[33] M.M. Abu-Khader, Plate heat exchangers: recent advances, Renew. Sust. Energy Rev. 16 (2012) 1883-1891.
[34] R.K. Shah, D.P. Sekulic, Fundamentals of Heat Exchanger Design, Hoboken: John Wiley & Sons (2003).
[35] Soudal, Calofer, Technical Data Sheet, Accessed on: 20 March, 2020, Available at: https://www.pfe.tech/wp-content/uploads/2017/02/Calofer-TDS-ID253.pdf, (2015).
[36] Y.A. Çengel, A.J. Ghajar, Heat and Mass Transfer 4th edition, New York: McGraw-Hill, (2011).
[37] J.P. Meyer, M. Everts, Single-phase mixed convection of developing and fully developed flow in smooth horizontal circular tubes in the laminar and transitional flow regimes, Int. J. Heat Mass Tran. 117 (2018) 1251-1273.
[38] M. Everts, J.P. Meyer, Flow regime maps for smooth horizontal tubes at a constant heat flux, Int. J. Heat Mass Tran. 117 (2018) 1274-1290.
[39] W.G. Le Roux, T. Bello-Ochende, J.P. Meyer, Optimisation of an open rectangular cavity receiver and recuperator used in a small-scale solar thermal Brayton cycle with thermal losses, In: Proceedings of 10th International Conference on Heat Transfer, Fluid Mechanics and Thermodynamics, Orlando, Florida (2014) 409-507.
[40] K.E. Dellar, W.G. Le Roux, J.P Meyer, Experimental testing of a small-scale solar thermal Brayton cycle recuperator, IHTC16-23587, International Heat Transfer Conference Proceedings, Beijing, China (2018).
[41] K.E. Dellar, W.G. Le Roux, J.P Meyer, Small-scale solar thermal Brayton cycle recuperator: experimental testing and heat loss analysis. In: Proceedings of the 5th Annual Southern Africa Solar Energy Conference (SASEC 2018), Durban, South Africa (2018).
[42] G.F. Nellis, J.M. Pfotenhauer, Effectiveness-NTU relationship for a counterflow heat exchanger subjected to an external heat transfer, J Heat Trans. 127 (2005) 1071-1073.
[43] W.C. Young, R.G. Budynas, Roark's Formulas for Stress and Strain, 7th edition, New York: McGraw-Hill (2002).
[44] C. Borgnakke, R.E. Sonntag, Fundamentals of Thermodynamics, 8th Edition, Michigan: Don Fowley (2013).